PERGAMON

International Journal of Heat and Mass Transfer 44 (2001) 1605–1618

International Journal of HEAT and MASS TRANSFER

www.elsevier.com/locate/ijhmt

Effects of buoyancy-driven convection on melting within spherical containers

J.M. Khodadadi *, Y. Zhang [1]

Department of Mechanical Engineering, Auburn University, 201 Ross Hall, Auburn, AL 36849-5341, USA

Received 13 August 1999; received in revised form 15 May 2000

Abstract

A computational study of the effects of buoyancy-driven convection on constrained melting of phase change materials within spherical containers is presented. The computations are based on an iterative, finite-volume numerical procedure using primitive-dependent variables, whereby the time-dependent continuity, momentum and energy equations in the spherical coordinate system are solved. A single-domain enthalpy formulation is used for simulation of the phase change phenomenon. The effect of phase change on convection is accounted for using a Darcy's law-type porous media treatment. Early during the melting process, the conduction mode of heat transfer is dominant, giving rise to concentric temperature contours. As the buoyancy-driven convection is strengthened due to the growth of the melt zone, melting in the top region of the sphere is much faster than in the bottom region due to the enhancement of the conduction mode of heat transfer. When buoyancy effects are very marked, as many as three time-dependent recirculating vortices are observed. In comparison to the diffusion-controlled melting, buoyancy-driven convection accelerates the melting process markedly. The Prandtl number plays an important role in the melting process. With the Rayleigh number fixed, changing the Prandtl number from 0.03 to 1.0 and 50 brings about totally different flow and melting patterns. The computational findings are verified through qualitative constrained melting experiments using a high-Prandtl number wax as the phase change material.

1. Introduction and literature review

The important role of buoyancy-driven convection during the phase change process has been recognized for some time now, and excellent reviews have been published [1–3]. In the metallurgical and material processing applications, it is well established that the properties of metals and alloys are determined by their microstructure, which in turn is strongly affected by the state of convection close to the solid–liquid interface during the melting or solidification processes. In thermal energy storage systems, capsules of spherical shape are one of the most commonly used for storing phase change materials (PCM). Although, the stimulus for research of melting and solidification processes is related to such advanced processing techniques such as spray casting, growth of defect-free crystals, latent heat-of-fusion storage system, etc., very little theoretical analysis of the phase change process in spherical geometries is available. Considering spherical geometries, apart from several analytical investigation of diffusion-controlled phase change processes reported before 1980s, Moore and Bayazitoglu [4] were the first to investigate the unconstrained melting (meaning that the solid portion drops within the melt due to its higher density) of the PCM within spherical enclosures both experimentally and numerically. A mathematical model was developed, which was based on the assumption that the bottom of the solid region melts so as to remain almost spherical. The polar velocity component within the gap was approximated as being similar to a pressure-induced flow between parallel plates, and the coefficients of the parabolic velocity profile in the gap were obtained by assuming that the solid and molten shell remain fixed

* Corresponding author. Tel.: +1-334-844-3333; fax: +1-334-844-3307.

E-mail address: jkhodada@eng.auburn.edu (J.M. Khodadadi).

[1] Currently with ICEM CFD, Livonia, Michigan, USA.

0017-9310/01/$ - see front matter
PII: S0017-9310(00)00192-7

Nomenclature

c_p	specific heat at constant pressure, J/(kg K)
C	porosity constant, kg/(m^3 s)
Da	Darcy number, defined as $\mu\lambda^3/CR^2(1-\lambda)^2$
g	gravitational acceleration, m/s^2
H	sensible enthalpy, J/kg
ΔH	latent heat, J/kg
k	thermal conductivity, W/(m K)
L	latent heat of fusion, J/kg
p	pressure, Pa
Pr	Prandtl number of the fluid, defined as ν/α
r	radial coordinate within the sphere, m
R	radius of the sphere, m
Ra	Rayleigh number, defined as $8g\beta(T_0-T_m)R^3/(\nu\alpha)$
Ste	Stefan number, defined as $c_p(T_0-T_m)/L$
t	time, s
T	temperature, K
T_i	initial temperature of the fluid, K
T_m	melting temperature of the phase change material, K
T_0	temperature of the container's surface, K
V_r	radial component of the fluid velocity, m/s
V_θ	polar component of the fluid velocity, m/s

Greek symbols

α	thermal diffusivity of the fluid, m^2/s
β	thermal expansion coefficient, K^{-1}
θ	polar angle in the sphere
λ	liquid volume fraction
μ	fluid viscosity, kg/(m s)
ν	kinematic viscosity, m^2/s
ρ	density, kg/m^3

Superscript

*	dimensionless quantities

and fluid is injected into the gap to produce the gap flow. With all the above assumptions, the initial stage up to about half the melting process was investigated. The interface position and temperature profiles for various Stefan numbers were given at various stages of melting. It was found that in the bulk melt region above the solid, convective motions arising from the dropping of the solid mass generally cannot be neglected. Bahrami and Wang [5] also investigated the melting process in a sphere. The velocity profile in the melt was obtained by assuming that the flow is similar to pressure-driven flow between parallel plates, and the heat transfer to the melting front is diffusion-controlled. Upon decoupling of the temperature field from the velocity field, an approximate closed-form solution of the melting process was obtained and the relationship between the interface properties and time was also given. Following along the lines of [4,5], Roy and Sengupta [6] obtained an analytical solution for the melting rate on the lower surface of the solid core. Later, Roy and Sengupta [7] studied the effects of natural convection within the thin melting layer in the bottom of the sphere and within the top part of the sphere during the unconstrained melting process. The two zones were analyzed separately but appropriate coupling conditions were utilized at the fluid–solid interface. They found that a significant amount of melting took place at the upper surface due to the significance of natural convection, whereas in previous research [4–6], the effect of natural convection on the melting process was neglected.

It is noteworthy to point out one more time that the convection considered in the above-mentioned literature is convection induced by the dropping of the solid core due to its greater density in comparison to the liquid phase. The only exception to this is the study of Roy and Sengupta [7] where the extra effect of natural convection was considered in the top fluid portion, and the heat transfer mechanism in the bottom half was diffusion-controlled. The "pure" buoyancy-driven convective effect – i.e., natural convection induced by temperature gradient in the melt – has not been investigated for spherical containers. Adetutu and Prasad [8] have recently reported their study of the effects of natural convection on the melting process inside a cylinder and their work further stimulated our ongoing investigation of transport phenomena in droplets and spherical containers, e.g., [9]. Given the status of the limited knowledge of constrained phase change during which the effects of buoyancy-driven convection can conveniently be analyzed without the complication of the movement of the solid portion, the present computational study was undertaken. A single-domain enthalpy formulation is utilized as opposed to earlier analyses which studied each phase separately. In addition, focus is placed on low-Prandtl number fluids, although the effects of the Prandtl number variation is also elucidated. In order to support the computational findings presented here, a qualitative study of the visualization of the constrained melting problem at hand was also carried out.

2. Mathematical model

The physical model considered here is that of a spherical container of radius R which holds a solid PCM at temperature T_i, which could be a temperature lower than the melting temperature (T_m), i.e., the phase change material could be *subcooled*. For time $t > 0$, a constant temperature (T_0) greater than the melting temperature is imposed on the surface of the sphere, i.e., $T_0 > T_m$.

Melting will initiate at the surface and the solid–liquid interface will move into the sphere. Emphasis is placed on analysis of constrained melting which means that both the solid and liquid phases have the same density. As a result, the density variation inside the liquid phase due to temperature gradients will promote buoyancy-driven convection and the solid portion will not move inside the liquid melt. The schematic diagram of the physical model is shown in Fig. 1.

2.1. Governing equations

Because of the imposed surface temperature, heat penetrates into the sphere's interior to melt the PCM, and as the temperature of the melt rises, a density change within the melt is expected, which then drives the buoyancy-driven convection. In this study the following assumptions are made:

1. Both the solid and the liquid phases are homogeneous and isotropic, and the melting process is axisymmetric.
2. Both phases at the solid–liquid interface are in thermal equilibrium (T_m).
3. Density change due to the phase change is neglected, thus the solid portion of the material is held rigid. The Boussinesq approximation is invoked, i.e., density change within the liquid phase which drives natural convection in the melt is only considered in the body force terms.

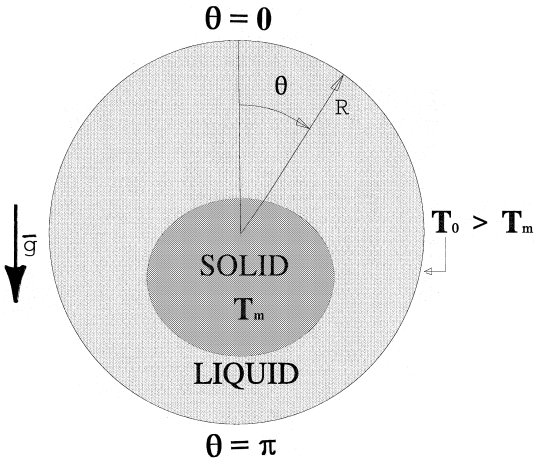

Fig. 1. Schematic diagram of melting within a spherical container.

Given these assumptions, the continuity, momentum and energy equations in the spherical coordinates for the phase change problem can be written in the form of general governing equation

$$\begin{aligned}&\frac{\partial(\rho\xi)}{\partial t}+\frac{1}{r^2\sin\theta}\frac{\partial}{\partial r}(\rho V_r r^2\sin\theta\,\xi)\\&\quad+\frac{1}{r^2\sin\theta}\frac{\partial}{\partial\theta}(\rho V_\theta r\sin\theta\,\xi)\\&\quad=\frac{1}{r^2\sin\theta}\frac{\partial}{\partial r}\left(\Gamma_\xi r^2\sin\theta\frac{\partial\xi}{\partial r}\right)\\&\qquad+\frac{1}{r^2\sin\theta}\frac{\partial}{\partial\theta}\left(\Gamma_\xi\sin\theta\frac{\partial\xi}{\partial\theta}\right)+S^\xi.\end{aligned}\tag{1}$$

The individual equations can be summarized in terms of ξ, Γ_ξ and S^ξ as shown in Table 1. The *enthalpy formulation* which is used in this study belongs to the single-region (or continuum) class of methods. The present form of the source term for the thermal energy equation in Table 1 can be derived by splitting the total enthalpy of the material into the sensible enthalpy ($H = c_p T$) and the latent heat (ΔH) [10]. A Darcy's law-type of porous medium treatment [10] is utilized to account for the effect of phase change on convection. In Table 1, the last components of the source term in the momentum equations are the Darcy damping terms which will conveniently force the velocity to zero in the solid phase. In the present study, since phase change of a pure material is our main concern, the last two components of the source term of the energy equation were neglected, since ΔH is constant in the solid and liquid phases, thus making the two terms negligible due to mass conservation. The details of the treatment of the source term of the energy equation is given by Zhang [11].

Table 1
Governing transport equations

Equation	ξ	Γ_ξ	S^ξ
Continuity	1	0	0
Polar direction momentum	V_θ	μ	$-\frac{1}{r}\frac{\partial p}{\partial\theta}-\rho g\beta(T-T_m)\sin\theta-\rho\frac{V_r V_\theta}{r}+\mu\frac{2}{r^2}\frac{\partial V_r}{\partial\theta}-\frac{\mu}{r^2\sin^2\theta}V_\theta-\frac{C(1-\lambda)^2}{\lambda^3}V_\theta$
Radial direction momentum	V_r	μ	$-\frac{\partial p}{\partial r}+\rho g\beta(T-T_m)\cos\theta+\rho\frac{V_\theta^2}{r}-\mu\frac{2}{r^2}\frac{\partial V_\theta}{\partial\theta}-\mu\frac{2\cot\theta}{r^2}V_\theta-2\frac{\mu}{r^2}V_r-\frac{C(1-\lambda)^2}{\lambda^3}V_r$
Thermal energy	H	$\frac{\mu}{Pr}$	$-\frac{1}{c_p}\frac{\partial(\Delta H)}{\partial t}-\frac{1}{c_p}\frac{1}{r^2}\frac{\partial}{\partial r}(r^2V_r\Delta H)-\frac{1}{c_p}\frac{1}{r\sin\theta}\frac{\partial}{\partial\theta}(V_\theta\Delta H\sin\theta)$

2.2. Boundary and initial conditions

The boundary and initial conditions to be satisfied for the present model are:

(i) No slip boundary condition and uniform imposed constant temperature are assumed on the surface of the sphere

$$V_r = V_\theta = 0, \quad T = T_0 \quad \text{at } r = R \quad \text{for } t > 0. \tag{2}$$

(ii) The problem associated with the variables being multi-valued at the center is removed by introducing a very small, but finite, interior surface. The validity of this technique was discussed by de Vahl Davis [12]. The axial symmetric boundary condition is applied at the interior surface. On all the boundaries of the computational domain, the gradient boundary conditions were discretized by using a three-point formula with second order of accuracy. The axisymmetric boundary condition along the $\theta = 0$ and π lines are also invoked, i.e.:

$$V_r = \frac{\partial V_\theta}{\partial \theta} = \frac{\partial T}{\partial \theta} = 0 \quad \text{at } \theta = 0, \pi. \tag{3}$$

(iii) The initial condition is:

$$V_r = V_\theta = 0, \quad T = T_\mathrm{i} \quad \text{at } t = 0. \tag{4}$$

2.3. Dimensionless governing equations

Introducing the following dimensionless variables:

$$\begin{aligned} &r^* = \frac{r}{R}, \quad V^* = \frac{R}{\alpha} V, \quad p^* = \frac{R^2}{\rho \alpha^2} p, \quad T^* = \frac{T - T_\mathrm{i}}{T_0 - T_\mathrm{i}} \\ &t^* = Ste\, \frac{\alpha t}{R^2}, \quad H^* = \frac{(H - H_\mathrm{i})}{L} = Ste \cdot Sb \cdot T^*, \end{aligned} \tag{5}$$

where the Stefan (Ste) and Subcooling (Sb) numbers are defined as

$$Ste = \frac{c_\mathrm{p}(T_0 - T_\mathrm{m})}{L}, \quad Sb = \frac{T_\mathrm{i} - T_0}{T_\mathrm{m} - T_0}, \tag{6}$$

the dimensionless governing equations are obtained. These are:

Mass conservation:

$$\nabla \cdot \vec{U}^* = 0, \tag{7}$$

Momentum equation:

$$Ste \frac{\partial \vec{U}^*}{\partial t^*} + \vec{U}^* \cdot \nabla^* \vec{U}^* = -\nabla^* p^* + Pr \nabla^{*^2} \vec{U}^* + \frac{1}{8} Ra\, Pr\, Sb\, T^* \vec{e}_g - \frac{Pr}{Da} \vec{U}^*, \tag{8}$$

where $\vec{U}^*, \vec{e}_g$ are the velocity vector and the unit vector in the direction of the gravitational acceleration (Fig. 1), respectively, and:

$$\begin{aligned} &Da = \frac{\mu \lambda^3}{C R^2 (1 - \lambda)^2}, \quad Pr = \frac{\nu}{\alpha}, \\ &Ra = \frac{8 g \beta (T_0 - T_m) R^3}{\nu \alpha}. \end{aligned} \tag{9}$$

The thermal energy conservation is

$$Ste \frac{\partial H^*}{\partial t^*} + \vec{U}^* \cdot \nabla^* H^* = \nabla^{*^2} H^* - Ste \frac{\partial \lambda}{\partial t^*}. \tag{10}$$

A linear relationship between the latent heat and temperature is used, i.e., $\Delta H = \lambda L$ [10], where L is the latent heat of fusion and the liquid volume fraction (λ) is given by

$$\lambda = \begin{cases} 1, & T \succ T_\mathrm{l}, \\ \frac{T - T_\mathrm{s}}{T_\mathrm{l} - T_\mathrm{s}}, & T_\mathrm{s} \preceq T \preceq T_\mathrm{l}, \\ 0, & T \prec T_\mathrm{s} \end{cases} \tag{11}$$

with T_l and T_s being the liquidus and solidus temperatures of an alloy, respectively. Finally, it should be noted that since $H^* = Ste\, Sb\, T^*$, Eq. (10) can also be expressed in terms of T^*.

The corresponding dimensionless boundary and initial conditions are:

Boundary conditions:

$$\begin{aligned} &V_r^* = V_\theta^* = 0, \quad T^* = 1, && \text{at } r^* = 1 \quad t^* > 0, \\ &\frac{\partial V_r^*}{\partial r^*} = \frac{\partial V_\theta^*}{\partial r^*} = \frac{\partial T^*}{\partial r^*} = 0 && \text{at } r^* \approx 0 \quad t^* > 0, \\ &V_r^* = \frac{\partial V_\theta^*}{\partial \theta} = \frac{\partial T^*}{\partial \theta} = 0 && \text{at } \theta = 0, \quad \pi \; t^* > 0. \end{aligned} \tag{12}$$

Initial condition:

$$V_r^* = V_\theta^* = 0, \quad T^* = 0 \quad \text{at } 0 < r^* < 1 \quad t^* = 0. \tag{13}$$

Obviously, the melting phenomenon at hand is shown to be a function of dimensionless spatial location (r/R and θ), dimensionless time ($t^* = Ste\, \alpha t / R^2$) and the dimensionless parameters, which are the Prandtl, Rayleigh, Stefan, Subcooling and Darcy numbers.

3. Computational details

The governing equations were solved using the semi-implicit method for pressure-linked equations (SIMPLE) procedure of Patankar [13]. A $121^r \times 41^\Theta$ grid system was found to be sufficient to resolve the details of the flow and temperature fields based on comparison of the streamline contours and liquid–solid interface positions for various grid densities. Forty-one (41) uniformly placed grids were laid in the polar angle direction extending from $\theta = 0$ to π and 121 uniform grids were laid in the radial direction. Fine grid distribution in the radial direction allowed the use of longer time steps and less under-relaxation in the simulation process. The

temporal derivatives were treated using an implicit formulation which demands no stability requirement. Depending on the operating conditions, the time step used in the computations was maintained fixed between 1 and 6 s, corresponding to dimensionless time step (Δt^*) $\sim 10^{-4}$. The relaxation factors were generally 0.1, 0.1, 0.1 and 0.1 for V_r, V_θ, P and T, respectively, whereas a relaxation factor of 0.15 was applied to the latent heat updating. At every time step, the iterations were terminated when the sum of the normalized absolute residuals for each variable was less than $\epsilon_1 = 10^{-8}$, and the relative change of all the variables at every grid point was assured to be lower than $\epsilon_2 = 10^{-5}$ upon convergence. At each time step, the number of iterations needed to achieve convergence varied between 100 and 5000. The CPU time per iteration was about 1.5×10^{-1} s. The computations were performed on the CRAY C-90 supercomputer of the Alabama Supercomputer Authority, which is located in Huntsville, Alabama.

4. Results and discussion

4.1. Thermophysical properties and process parameters

In the present study, emphasis was placed on low-Prandtl number fluids which is typical of most molten liquid metals and alloys. In view of this, silicon was chosen as a typical low-Prandtl number fluid and its thermophysical properties were used [8] in the simulation process. These are:

$$k = 50\ \mathrm{W/(m\ K)}, \quad \rho = 2420\ \mathrm{kg/\ m^3},$$
$$c_p = 960\ \mathrm{J/(kg\ K)}, \quad L = 1.8 \times 10^6\ \mathrm{J/kg}, \qquad (14)$$
$$Pr = 0.03, \quad \beta = 1.384 \times 10^{-4}\ \mathrm{K^{-1}}.$$

For a given material (fixed Prandtl number), the Stefan and Rayleigh numbers cannot be varied independently. Therefore, a parametric study by which combinations of the radius of the sphere (R) and the temperature differential ($\Delta T = T_0 - T_m$) were varied was undertaken in order to assess the role of buoyancy-driven convection during melting. Moderate Prandtl number ($Pr = 1.0$) and high-Prandtl number ($Pr = 50$) fluids were also considered. Table 2 gives the pertaining process parameters for the computed cases. The subcooling effects were not included in the simulation process, i.e., the initial temperature of the phase change material was assumed to be at the melting temperature ($Sb = 1$). In order to simulate the phase change process of the pure materials, the mushy zone is made very small. For the present study, ($T_l - T_s$) was given the value of 0.5°C in the production runs for the simulation material (Si) which has a melting temperature of 1685 K. Meanwhile the porosity constant C in the Darcy number is set to 10^9 kg/(m^3 s), so that the momentum equations drive the velocity to zero in the solid zone [8,10].

4.2. Diffusion-controlled melting

For benchmarking purposes, a set of simulations considering only the diffusion-controlled melting was undertaken. For these cases, a uniform radial grid system (100–200 grid points) was utilized. In the absence of convection effects, diffusion-controlled melting is independent of the angular position and the unmelted portion remains a perfect sphere at all times with the radial position of the liquid–solid interface decreasing with time. Concentric temperature contours are another feature of diffusion-controlled melting. The time span needed to melt the material due to conduction mode of heat transfer only is summarized in column 5 of Table 2. It is noted that the dimensionless total melting times (t^*_{fm}) are nearly constant at about 0.165. These time spans were used to get a conservative estimate for the duration of the convection phase of the computations.

4.3. Transient fluid flow and temperature fields – effect of the Rayleigh number

In order to assess the role of the Rayleigh number on the melting process, several cases were run as summarized in Table 2. When the Rayleigh number is small ($Ra \sim 10^4$), buoyancy-driven convection almost plays no role in the melting process. The contours of the temperature field feature concentric ring-like patterns and the interface at different angular locations recess almost at the same rate. This is also indicated by virtually no difference in the total melting time between the

Table 2
Computational cases studied ($Pr = 0.03$)

ΔT [°C]	R [m]	Rayleigh number	Stefan number	Conduction-only melting time [s/dimensionless]	Convection melting time [s/dimensionless]
15	0.01	1.269×10^4	0.008	92/0.158	92/0.158
50	0.015	1.428×10^5	0.0267	65.5/0.167	60/0.153
50	0.03	1.143×10^6	0.0267	262/0.167	228/0.145
50	0.065	1.151×10^7	0.0267	1206/0.165	750/0.102
100	0.05	1.048×10^7	0.0533	370/0.170	210/0.098

conduction-only case and the convection enhanced case shown in the first row of Table 2.

4.3.1. Flow structure for different Rayleigh numbers

Case (*a*) ($Ra = 1.428 \times 10^5$): Instantaneous contours of the streamline and temperature fields are given in Fig. 2 for a $\Delta T = 50$°C and $R = 0.015$ m case (Rayleigh and Stefan numbers of 1.428×10^5 and 0.0267, respectively). Four instantaneous plots are provided at dimensionless times $t^* = 0.026, 0.077, 0.128$ and 0.153. The temperature contours are shown on the right half of each circle whereas the streamlines are presented on the left half with the $\theta = 0$ and π vertical line separating the two fields. The shaded area indicates the unmelted solid phase at a given instant. Early on during the melting process, the temperature contours are nearly perfect concentric rings indicating the dominance of the conduction mode of heat transfer (Fig. 2(a)). Due to the small radius of the sphere, the Rayleigh number is relatively low for this case and the established buoyancy-driven convection is not strong in comparison to conduction. Note that around $t^* = 0.077$, the temperature contours begin to deviate from concentric ring patterns and the solid unmelted zone is shaped as an oblate spheroid (Fig. 2(b)), indicating that convection begins to affect the melting process. When the melting process reaches a point where the whole domain is nearly completely melted ($t^* \approx 0.153$ for this case), the solid zone is found at $r/R \sim 0.2$ below the center of the sphere (Fig. 2(d)), suggesting that melting has been more intense in the top portion of the sphere. Fig. 3 shows the history of the maximum and minimum stream function values in the melt. In the present study, the stream function is set to be zero on the surface of the sphere. The maximum stream function represents the strength of the clockwise-rotating recirculating cell of Fig. 2, while the minimum stream function represents the strength of the weak counter-clockwise rotating recirculating cell which appears around $t^* \sim 0.065$. In the beginning, fluid flow is weak with a single recirculating fluid cell spreading all over the thin spherical annulus. As the melting process marches on, fluid flow gets stronger with the maximum stream function value rising in time, and reaches approximately its extreme value around $t^* \sim 0.05$. At a certain time, $t^* \sim 0.065$ for this

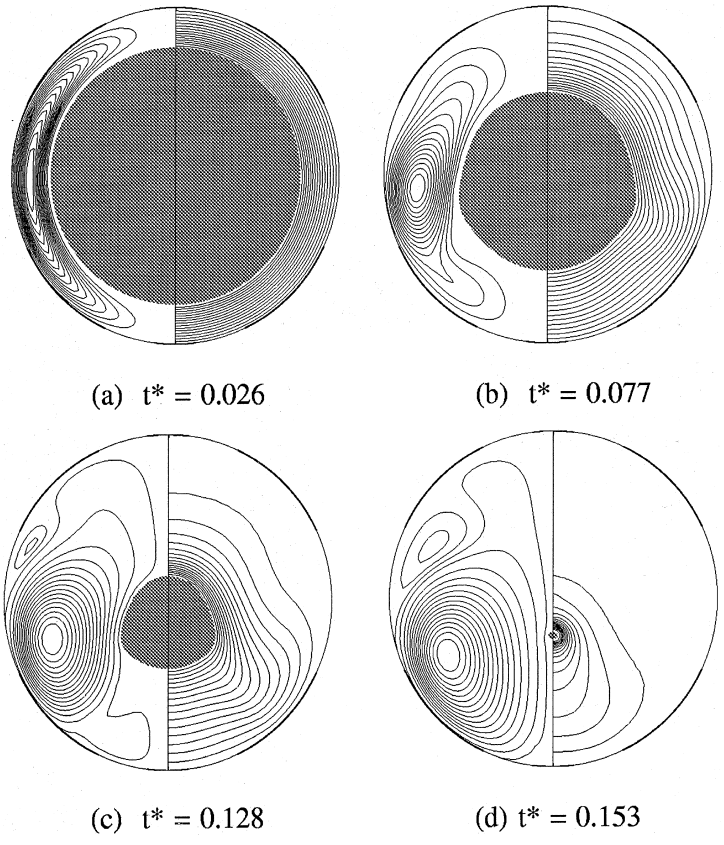

Fig. 2. Streamlines and temperature contours for $\Delta T = 50$°C and $R = 0.015$ m ($Ra = 1.428 \times 10^5$, $Ste = 0.0267$ and $Pr = 0.03$) at different time instants.

case, a second counter-clockwise-rotating recirculating fluid cell at the top portion ($\theta \approx 45°$) of the melt is induced due to the skewed temperature field.

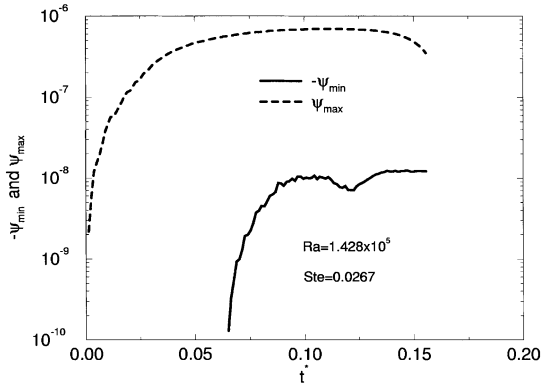

Fig. 3. The time history of the minimum and maximum stream function values (Case (a)).

Case (*b*) ($Ra = 1.143 \times 10^6$): Contours of the streamline and temperature fields for a $\Delta T = 50°C$ and $R = 0.03$ m case (Rayleigh and Stefan numbers of 1.143×10^6 and 0.0267, respectively) are given in Fig. 4 for four dimensionless time instants ($t^* = 0.026$, 0.077, 0.102 and 0.128). At the time instant $t^* = 0.026$ in Fig. 4(a), the temperature contours are still nearly concentric suggesting the dominance of the conduction mode of heat transfer. As the melting process continues, the fluid heated near the surface rises to the top replacing the colder fluid. The displaced colder fluid drops in the same direction of gravity and enhances the already-existing conduction heat transfer. This will in turn cause the top portion of the sphere ($\theta \approx 0°$) to melt faster than the rest of the sphere. The cold fluid dropping down along the solid–liquid interface finally arrives at the bottom of the solid zone. In the bottom region ($\theta \approx 180°$), the convective mode of transfer counteracts conduction of heat from the surface toward the unmelted region. As a result, the melting rate in the bottom region should be slower than any other region within the

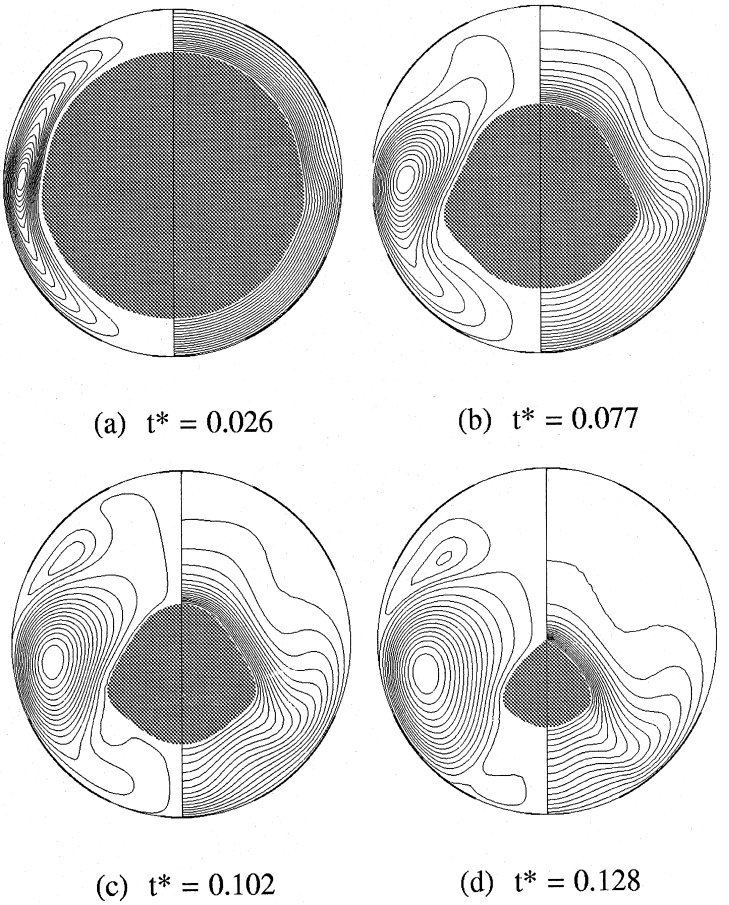

Fig. 4. Streamlines and temperature contours for $\Delta T = 50°C$ and $R = 0.03$ m ($Ra = 1.143 \times 10^6$, $Ste = 0.0267$ and $Pr = 0.03$) at different time instants.

sphere. The consequence of these effects are clearly observed in Fig. 4(b) ($t^* = 0.077$). As the melting is continued and the convection effects are enhanced, temperature contours start to deviate markedly from concentric-ring-like patterns. The skewed temperature contours in the top zones ($\theta \approx 45°$) of the sphere give rise to a new recirculating structure at a much earlier time ($t^* \approx 0.03$). The presence of a similar phenomenon has been reported by Adetutu and Prasad [8] for melting within a horizontal cylinder. For this case, near the completion of the melting period ($t^* = 0.145$), the solid zone is found at $r/R \sim 0.3$ below the center of the sphere (not shown in Fig. 4), indicating more intense melting in the top portion of the sphere than in Case (a). Fig. 5 shows the maximum and minimum stream function values in the melt. It is noted that the second, counter-clockwise-rotating recirculating cell is relatively stronger (only about one order of magnitude difference in the value of stream functions between the two cells) and appears much earlier ($t^* \sim 0.03$) when compared to Case (a). The time-dependent positions of the eyes of the two recirculating cells for this case and others are not given here but have been discussed by Zhang [11].

Case (*c*) ($Ra = 1.151 \times 10^7$): Contours of the instantaneous streamline and temperature fields are given in Fig. 6 for a $\Delta T = 50°C$ and $R = 0.065$ m case (Rayleigh and Stefan numbers of 1.151×10^7 and 0.0267, respectively) at dimensionless times $t^* = 0.0245$, 0.0367, 0.0611, 0.0734, 0.0978 and 0.1028. This case represents a relatively high Rayleigh number, so the effects of buoyancy-driven convection are more pronounced compared to previous cases discussed above. With the temperature contours getting skewed at an earlier time, the new recirculating vortices are seen earlier in the top and bottom regions in Figs. 6(d) and (e). These vortices maintain their location and strength for some time. As the unmelted portion gets smaller, the temperature skewedness in the bottom region is relaxed and the bottom vortex is consumed into the long-lived original vortex (Fig. 6(f)). Near the completion of the melting period ($t^* = 0.1028$), the solid zone is found to drop down further to $r/R \sim 0.35$ below the center of the sphere, indicating an even stronger convective role in the melting process than that in Cases (a) and (b). Fig. 7 shows the time history of the maximum and minimum stream function values for three recirculating cells in the melt. Since the Rayleigh number is high, fluid motion is stronger, which can be seen from the absolute values of the maximum stream functions in the above-mentioned three cases. The second cell appears at $t^* \approx 0.01$, whereas the third cell appears at $t^* \approx 0.065$.

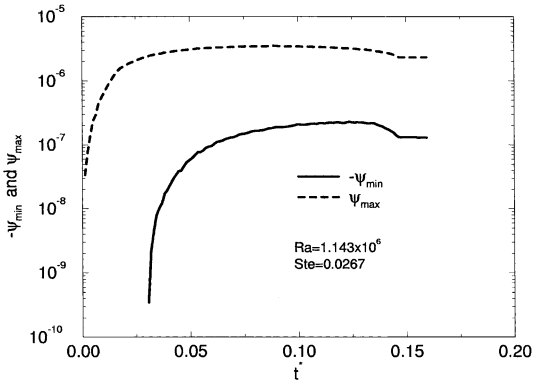

Fig. 5. The time history of the minimum and maximum stream function values (Case (b)).

4.3.2. Position of the liquid–solid interface

The effects of buoyancy-driven convection on preferential melting of the sphere at different points are more clearly elucidated by presenting the instantaneous location of the melt front. This information is given in Fig. 8(a) for Case (b), where the dimensionless radial location of the melt interface ($r^* = r/R$) at three angular positions ($\theta = 0°$, 90° and 180°) are given as functions of the dimensionless time, t^*. The angle-independent radial position of the melt for the case of diffusion-controlled melting is also shown for comparison purposes. As outlined above, the top region of the sphere ($\theta = 0°$ melts faster than the rest of the sphere. For this specific case, the bottom region ($\theta = 180°$) melts slowest even when compared to the case of pure conduction, whereas melting along the horizontal plane going through the center ($\theta = 90°$) is faster than the case of diffusion-controlled melting. The dimensionless radial locations of the melt interface at the same three angular positions are given as functions of the dimensionless time in Fig. 8(b) for Case (c). For this case, the effect of buoyancy-driven convection is the most marked and melting times in terms of the dimensionless variable t^* are small. It is observed that the melt fronts at the angular positions of $\theta = 0$ and 90° disappear about 35% faster when compared to their counterparts in Fig. 8(a). The evolution of the melting process near the bottom ($\theta = 180°$) is somehow different when compared to that of Fig. 8(a). Early on during the process, the melting is slow compared to the diffusion-controlled case, due to the counteraction of convection and conduction in that region. Around $t^* = 0.06$, with the emergence of the two new vortex structures the melting is intensified to a rate faster than that in the case of diffusion-controlled melting. For comparison, the dimensionless radial locations of the melt interface at the same three angular positions are also given as functions of the dimensionless time in Fig. 8(c) for Case (a). The Rayleigh number for this case being the smallest among the three cases studied, the melting pattern deviates very little in comparison to diffusion-controlled melting.

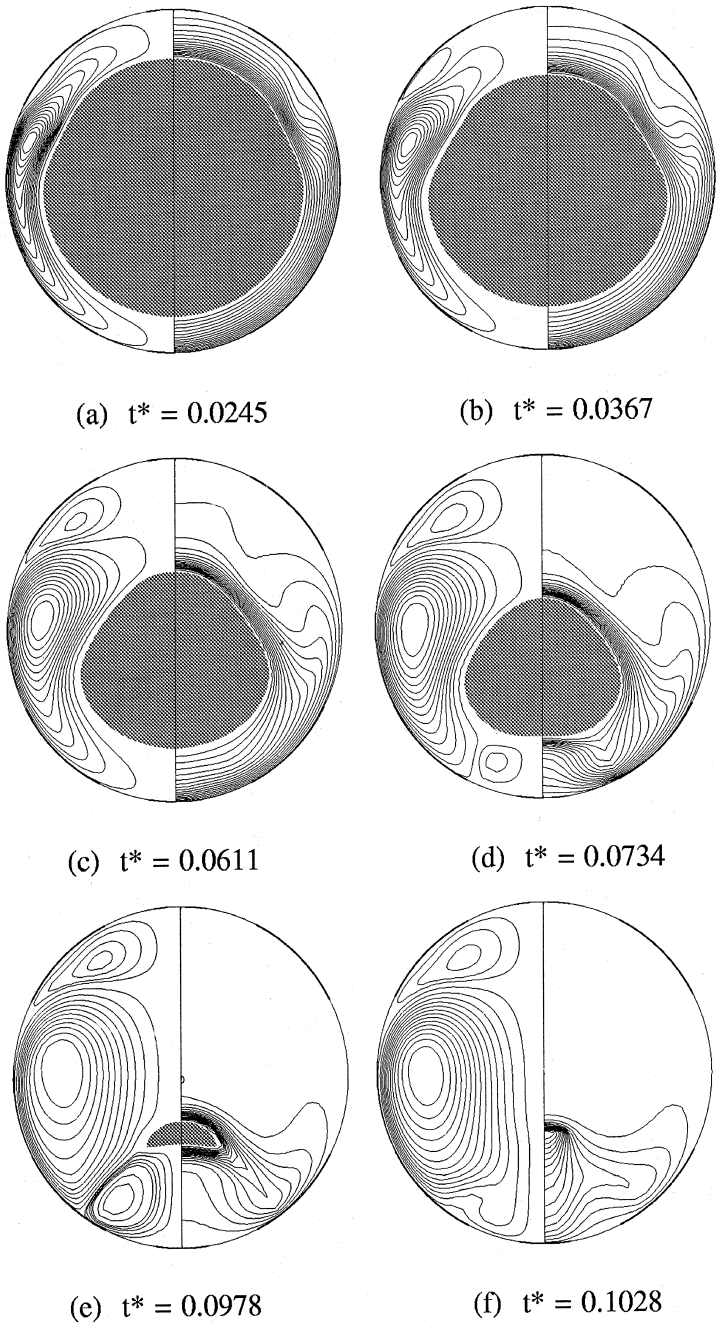

Fig. 6. Streamlines and temperature contours for $\Delta T = 50$°C and $R = 0.065$ m ($Ra = 1.151 \times 10^7$, $Ste = 0.0267$ and $Pr = 0.03$) at different time instants.

4.4. Total melting time – comparison to diffusion-controlled melting

In order to assess the overall role of convection on the melting process, the instantaneous total liquid volume fractions for the three Cases (a)–(c) are plotted in Fig. 9. The liquid volume fraction (LVF), which is the ratio of the melt volume to the total volume of the sphere, was determined from a numerical integration of the local volume fraction, λ, i.e.,

$$\mathrm{LVF}(t) = \frac{1}{(4/3)\pi R^3} \int_0^{\pi} \int_0^{R} \lambda(r,\theta,t) r^2 \sin\theta \, \mathrm{d}r \, \mathrm{d}\theta. \quad (15)$$

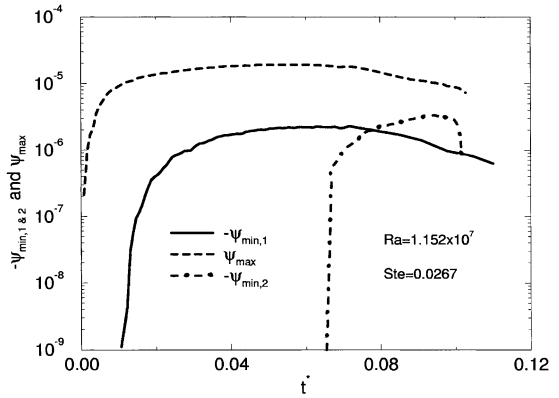

Fig. 7. The time history of the minimum and maximum stream function values (Case (c)).

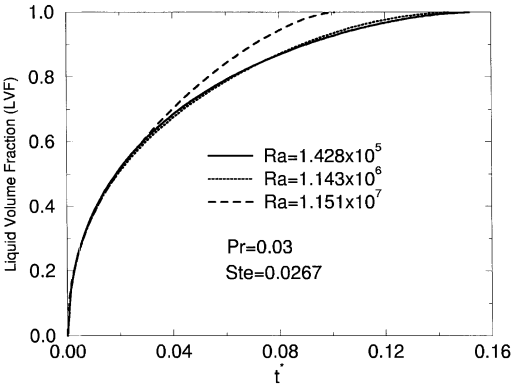

Fig. 9. Transient evolution of total liquid volume fraction for Cases (a), (b) and (c).

The total melting time was 8% shorter for Case (a), 15% shorter for Case (b), and 40% shorter for Case (c) when compared to the corresponding diffusion-controlled melting processes. The higher the Rayleigh number, the bigger the deviation from the diffusion-controlled melting. The total melting times are also summarized in column 6 of Table 2.

4.5. Effect of the Stefan number

In order to get an understanding of the role of the Stefan number during the melting process, another case comparable to Case (c) was run, and the process parameters for this case are listed in the last row of Table 2. In order to isolate the effect of the Stefan

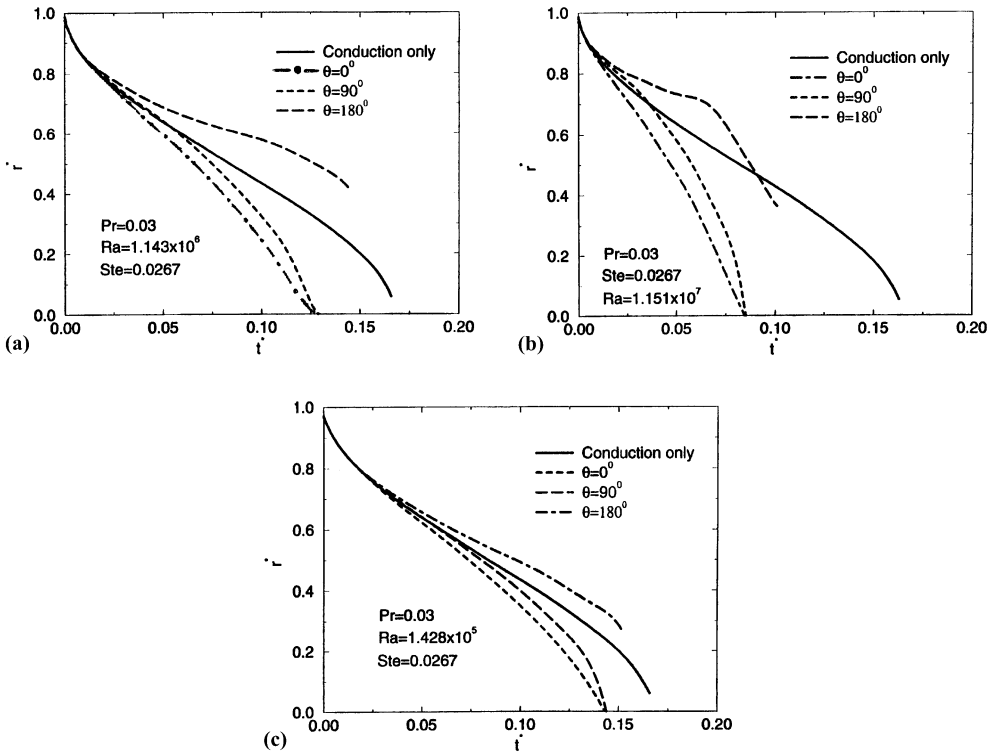

Fig. 8. The time history of the radial position of the melt interface for: (a) Case (b); (b) Case (c); (c) Case (a).

number, the Prandtl number was kept constant. The Rayleigh number was approximately kept unchanged by manipulating the ΔT and R combination, and the Stefan number was changed from 0.0267 to 0.0533. Upon comparison of the results for this case to those of Case (c), it was concluded that the flow and thermal fields are very similar for both cases [11]. The radial position of the interface for the two cases showed virtually no difference. Although, it is premature to conclude that the Stefan number plays no role in the melting process due to the insufficient data, it is safe to say that the Rayleigh number has a greater impact on fluid flow than the Stefan number, at least in this range of Stefan numbers studied. This finding is in concert with the study of Adetutu and Prasad [8].

4.6. Effect of the Prandtl number

The Prandtl number is a measure of the relative significance of the momentum and thermal diffusivities. It is not possible to perform a parametric study of the effect of the Prandtl number, since the Rayleigh number changes simultaneously with any change in material properties, even if all the other process parameters are kept constant. Therefore, two hypothetical cases where the Prandtl numbers were arbitrarily set to 1.0 and 50 were simulated. This was done with the other process parameters changed so as to keep the Rayleigh and Stefan number similar to the Case (b). Fig. 10 shows the isotherms and streamlines as well as the solid–liquid interface for the case of $Pr = 1.0$. Comparison of the two cases ($Pr = 0.03$, Fig. 4 and $Pr = 1.0$, Fig. 10) indicates significant variations in the flow pattern and the shape of melt front. The solid core for the $Pr = 1.0$ case retains its spherical shape throughout the melting process, and the flow pattern consists of a single recirculating cell. The total melting time is $t^* = 0.112$ for this case, which in comparison to the conduction-only melting, is 32% faster, suggesting an even stronger overall convective effect on the melting process when compared to Case (b) (15%). Near the completion of the melting period, the solid core is found at $r/R = 0.486$

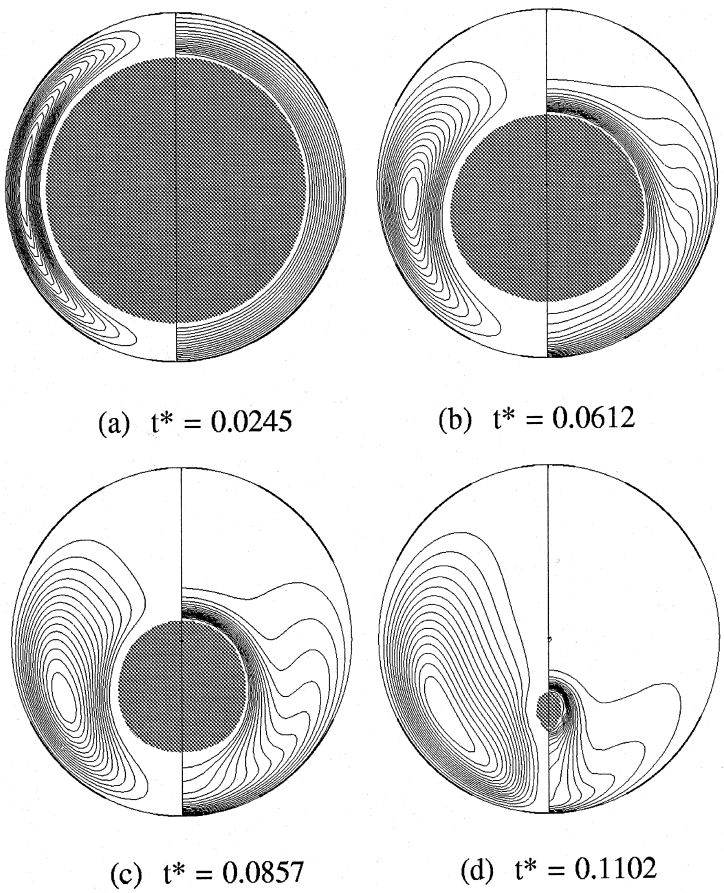

Fig. 10. Streamlines and temperature contours for $\Delta T = 50$°C and $R = 0.0925$ m ($Ra = 1.072 \times 10^6$, $Ste = 0.0267$ and $Pr = 1.0$) at different time instants.

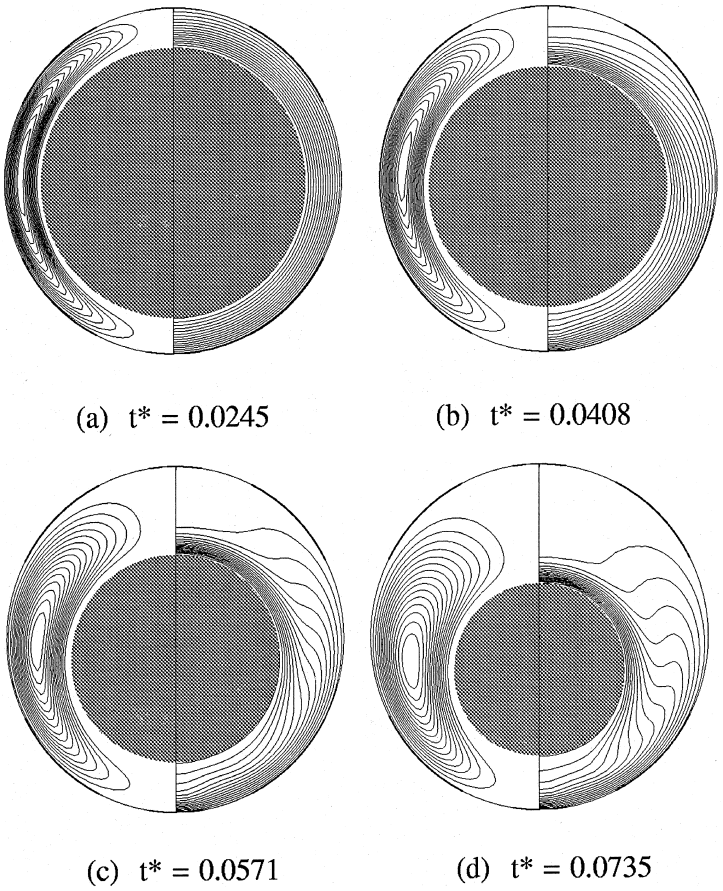

Fig. 11. Streamlines and temperature contours for $\Delta T = 50$°C and $R = 0.075$ m ($Ra = 1.072 \times 10^6$, $Ste = 0.0267$ and $Pr = 50$) at different time instants.

below the center of the sphere, indicating the greatest effect of natural convection among the cases discussed to this point.

The streamlines and temperature contours for the hypothetical case of $Pr = 50$ are given in Fig. 11. In general, the flow patterns are similar to the $Pr = 1.0$ case with the intense effect of natural convection causing preferred melting in the top portion, even though the spherical shape of the solid is maintained. Moreover, in comparison to the $Pr = 1.0$ case, the overall melting rate has been enhanced.

4.7. Visualization of the melting pattern

In order to support the validity of the computational findings presented above, a set of melting experiments were conducted. An aquarium was filled with water and it served as the hot fluid bath within which the spherical container holding the PCM was placed. The water heater was a Cole-Parmer PolyStat Model 1253-00 circulator (maximum power output of 1050 W), providing an even temperature distribution within water. Spherical light bulbs (GE Silvanus) with wall thickness of 0.65 mm and outside diameters of 51.5, 78.1, 94.0 and 123 mm were employed. The neck of each bulb was carefully cut off and the incandescent element and bulb threads were removed. Hollow cylindrical extensions were attached to the open neck of the bulbs in order to accommodate the expansion of the fluid upon melting and also provide a holding surface. A vertically-positioned long piece of jute packing twine was glued to the inside center bottom of every bulb which served as the PCM constraining agent. Each bulb was filled with a commercially available refined beeswax which served as the PCM. The Prandtl number of the PCM is estimated to be around 57 which is common for family of waxes. This PCM has a melting point range of 62–64°C and transforms from an opaque white–yellow color to a yellow-tinged transparent liquid upon melting. In order to avoid the problem of inhomogenity due to the entrapment of dissolved air in the wax, each bulb was filled with molten

wax and then allowed to solidify in a low-pressure (25 mm Hg vacuum) chamber over a period of 6–7 h. During each experiment, the bulb was placed in the aquarium and the water was slowly heated to 60°C. Once the PCM was isothermal at 60°C, temperature of the bath was ramped to 73°C (10°C above the melting point of the PCM). This scheme was preferred to the earlier attempts in which the colder bulb was suddenly introduced into the hot water and many bulbs cracked because of the thermal shock. Setting of the stop watch began when it was apparent that melting had started. This usually took place at the water temperature roughly equal to 70°C, but no gross melting occurred until the temperature of the bath had been maintained at 73°C for about 4–5 min. The photographs showing the images of a bulb at different time instants are given in Fig. 12. In

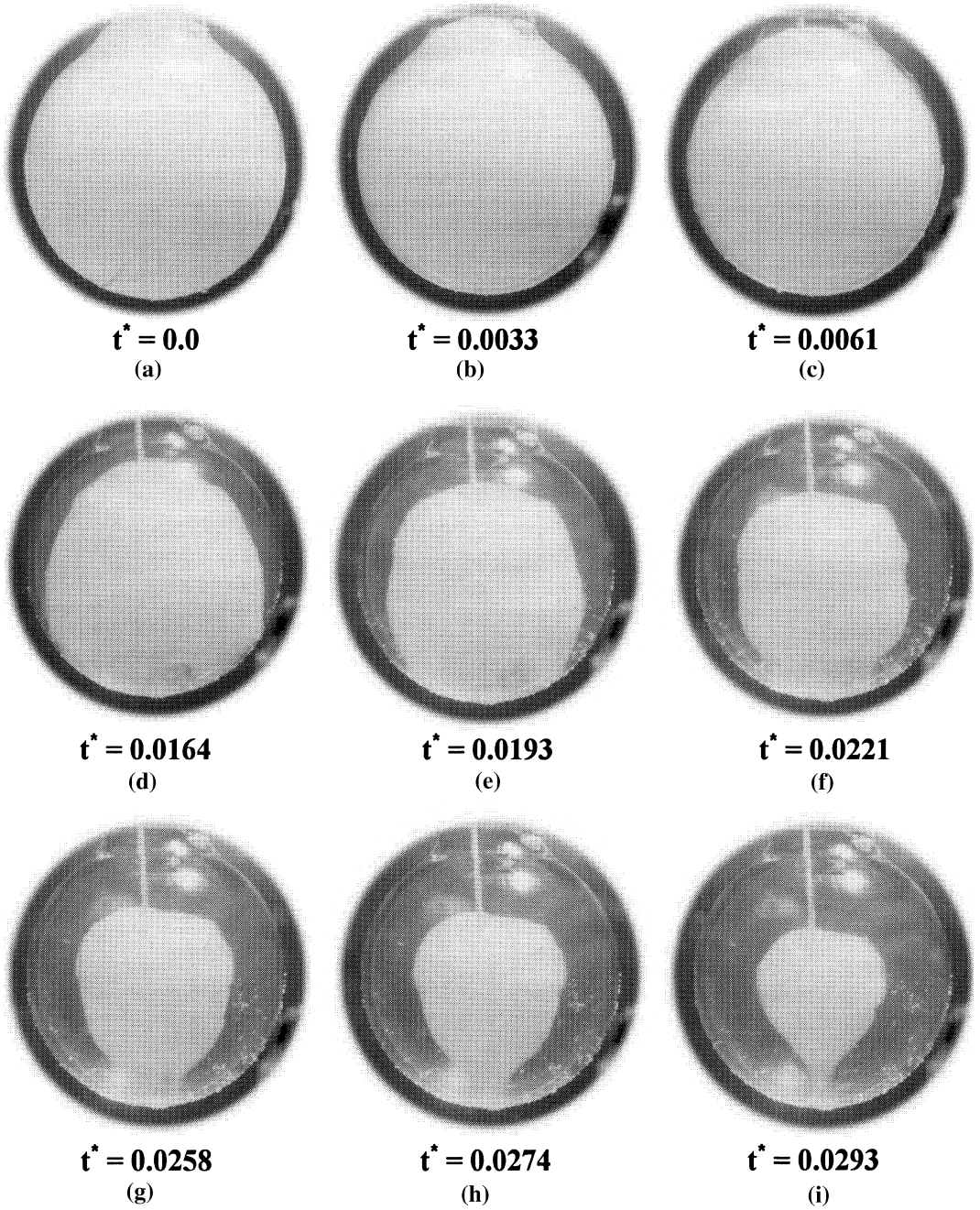

Fig. 12. Instantaneous photographs of the melting of wax inside a spherical bulb.

this figure, the inside bulb diameter was 92.7 mm and the Rayleigh and Stefan numbers were estimated to be 1.98×10^7 and 0.089, respectively. The estimated dimensionless time instants ($t^* = Ste\ \alpha t/R^2$) for each image are also identified. For conversion purposes, note that the actual time needed to melt the PCM to the pattern shown at time $t^* = 0.0293$ was $t = 134$ min after setting of the stop watch. Visual inspection of the images suggests that the general features of the melting phenomena uncovered by the mathematical model are physically present in the experiments. Early on, the melting is confined to a very thin layer next to the wall and the molten wax rises to the top and starts filling the cylindrical extension. Starting around $t^* = 0.0164$, the preferential melting on the top portion of the sphere due to buoyancy-driven convection is clearly established.

5. Conclusions

Based on the findings of the present computational study of the combined conduction and buoyancy-driven melting within a sphere, the following conclusions are drawn:

1. Early during the melting process, the conduction mode of heat transfer is dominant, giving rise to concentric temperature contours.
2. As the buoyancy-driven convection is strengthened due to the growth of the melt zone, it is observed that melting in the top region of the sphere is much faster than in the bottom region of the sphere. This is explained in terms of enhancement or impedance of the conduction mode of heat transfer at the respective locations.
3. When buoyancy effects are very marked, as many as three time-varying recirculating vortices are observed due to the skewedness of the temperature fields.
4. The strength of natural convection in the melting process is more clearly indicated by the Rayleigh number than the Stefan number, as the flow pattern and overall convective effects change markedly with the Rayleigh number.
5. The Prandtl number plays an important role in the melting process. With the Rayleigh number fixed, changing the Prandtl number from 0.03 to 1.0 and 50 bring about totally different flow and melting patterns.
6. The computational findings that the preferential melting on the top portion of the sphere is due to buoyancy-driven convection is clearly established through an experimental visualization of the melting of a commercial grade wax inside spherical bulbs.

Acknowledgements

The second author (YZ) acknowledges the financial support of the Mechanical Engineering Department at Auburn University through a teaching assistantship. Both authors are grateful to Mr. Richard Howe (currently a graduate student at Georgia Institute of Technology), who performed the visualization studies as part of a special project course during his undergraduate studies at Auburn University. The authors greatly acknowledge the support of the Alabama Supercomputer Authority by providing computing time on their supercomputer.

References

[1] J. Crank, Free and Moving Boundary Problems, Oxford University Press (Clarendon), London and New York, 1984.
[2] R. Viskanta, Heat transfer during melting and solidification of metals, Transactions of the ASME, J. Heat Transfer 110 (1988) 1205–1219.
[3] V.R. Voller, C.R. Swaminathan, B.G. Thomas, Fixed grid techniques for phase change problems: a review, Int. J. Numer. Meth. Eng. 30 (1990) 875–898.
[4] F.E. Moore, Y. Bayazitoglu, Melting within a spherical enclosure, Transactions of the ASME, J. Heat Transfer 104 (1982) 19–23.
[5] P.A. Bahrami, T.G. Wang, Analysis of gravity and conduction-driven melting in a sphere, Transactions of the ASME, J. Heat Transfer 109 (1987) 806–809.
[6] S.K. Roy, S. Sengupta, The melting process in spherical enclosures, Transactions of the ASME, J. Heat Transfer 109 (1987) 460–462.
[7] S.K. Roy, S. Sengupta, Gravity-assisted melting in a spherical enclosure: effects of natural convection, Int. J. Heat Mass Transfer 33 (1990) 1135–1147.
[8] O. Adetutu, V. Prasad, Effects of buoyancy on melting in a horizontal cylinder, in: Transport Phenomena in Materials Processing and Manufacturing, HTD, vol. 196, ASME, NY, 1992, pp. 125–134.
[9] Y. Zhang, J.M. Khodadadi, F. Shen, Pseudosteady-state natural convection inside spherical containers partially filled with a porous medium, Int. J. Heat Mass Transfer 42 (1999) 2327–2336.
[10] V.R. Voller, C. Prakash, A fixed grid numerical modelling methodology for convection–diffusion mushy region phase-change problems, Int. J. Heat Mass Transfer 30 (1987) 1709–1719.
[11] Y. Zhang, Transport phenomena with phase change inside droplets and spherical containers, Ph.D. Thesis, Auburn University, Auburn, Alabama, 1998.
[12] G. deVahl Davis, A note on a mesh for use with polar coordinates, Numer. Heat Transfer 2 (1979) 261–266.
[13] S.V. Patankar, Numerical Heat Transfer and Fluid Flow, Hemisphere Publishing, Washington, DC, 1980.